Article

Co-assembled MoS₂–TiO₂ Inverse Opal Photocatalysts for Visible Light-Activated Pharmaceutical Photodegradation

Stelios Loukopoulos, Elias Sakellis, Marios G. Kostakis, Dimitrios-Triantafyllos Gerokonstantis, Polychronis Tsipas, Spiros Gardelis, Athanassios G. Kontos, Fotis K. Katsaros, Zili Sideratou, George Em. Romanos, Athanasios Dimoulas, Nikolaos S. Thomaidis, and Vlassis Likodimos*

Read Online

ACCESS | Metrics & More | Article Recommendations | SI Supporting Information

ABSTRACT: Heterostructured photocatalytic materials in the form of photonic crystals have been attracting attention for their unique light harvesting ability that can be ideally combined with judicious compositional modifications toward the development of visible light-activated (VLA) photonic catalysts, though practical environmental applications, such as the degradation of pharmaceutical emerging contaminants, have been rarely reported. Herein, heterostructured MoS₂–TiO₂ inverse opal films are introduced as highly active immobilized photocatalysts for the VLA degradation of tetracycline and ciprofloxacin broad-spectrum antibiotics as well as salicylic acid. A single-step co-assembly method was implemented for the challenging incorporation of MoS₂ nanosheets into the nanocrystalline inverse opal walls. Compositional tuning and photonic band gap engineering of the MoS₂–TiO₂ photonic films showed that integration of low amounts of MoS₂ nanosheets in the inverse opal framework maintains intact the periodic macropore structure and enhances the available surface area, resulting in efficient VLA antibiotic degradation far beyond the performance of benchmark TiO₂ films. The combination of broadband MoS₂ visible light absorption and photonic-assisted light trapping together with the enhanced charge separation that enables the generation of reactive oxygen species via firm interfacial coupling between MoS₂ nanosheets and TiO₂ nanoparticles is concluded as a competent approach for pharmaceutical abatement in water bodies.
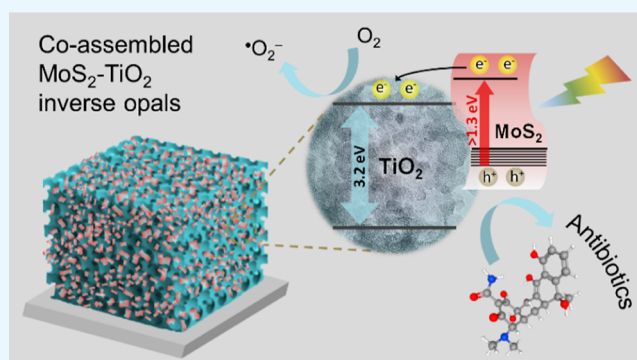
1. INTRODUCTION

Nanostructured titanium dioxide (TiO₂) materials have been attracting continuous attention as benchmark low-cost photocatalysts due to their high oxidation/reduction capacity, photochemical stability, and low toxicity.[1] However, practical applications are impeded by the wide band gap (3.0−3.2 eV) of TiO₂, which absorbs in the UVA spectral range, accounting for only 4−5% of the sun's total irradiation, and the persistent charge carrier recombination. Intensive research efforts have been accordingly devoted to mitigating these intrinsic material's limitations by electronic-based modifications, the most prominent being defect engineering[2,3] and heterostructuring of TiO₂ with narrow band gap semiconductors such as the unique graphitic carbon nitride (g-C₃N₄) polymeric photocatalyst,[4,5] which can simultaneously promote visible light absorption and charge separation for TiO₂ nanomaterials as standalone photocatalysts or assisted by suitable electron scavengers such as persulfate reagents.[6] In addition, structural/morphological modifications have been put forward in order to improve the performance of TiO₂ photocatalysts, the most favorable being TiO₂ nanostructuring in the form of mesoporous materials that offer an interconnected pore network, which increases surface area and the amount of reaction sites while assisting molecular diffusion during the photocatalytic reaction.[7,8] A direct, yet challenging morphology-based approach to enhancing light trapping is by shaping TiO₂ nanomaterials in the form of photonic crystals (PCs), the most conspicuous structures to control light−matter interactions.[9] PC-assisted photocatalysis has emerged as an advanced modification for improving light harvesting by photocatalytic nanomaterials, especially TiO₂ photocatalysts, at frequencies of weak materials' electronic absorption by slow light propagation primarily at the edges of the photonic band gap (PBG).[10,11] These distinctive structural features of PC catalysts, the most common being inverse opals, come along with the enhanced molecular transport and adsorption capacity of meso-macroporous structures and can be further combined

with rational compositional modifications for the development of visible light-activated (VLA) photonic catalysts.[12]

Among diverse modification approaches, heterostructuring TiO_2 with molybdenum disulfide (MoS_2) nanosheets, the prototypical two-dimensional (2D) layered transition-metal dichalcogenide,[13] has emerged as a promising route to an environmentally benign, composite photocatalyst that features broadband visible light activation with enhanced charge separation.[14,15] Decreasing the thickness of the thermodynamically stable semiconducting 2H MoS_2 phase down to a single layer leads to an indirect-to-direct band gap transition from the bulk value of 1.3 to 1.9 eV,[16] reflecting quantum size effects that underlie the marked variation of the interaction between Mo d orbitals and S antibonding p_z orbitals with the van der Waals interlayer coupling.[17] This unique tunability together with the excellent electrical, optical, and mechanical properties of 2D MoS_2 underpinned its application potential beyond electronics and optoelectronics[18] to photocatalytic and electrocatalytic H_2 evolution,[19] as well as water-related environmental applications including organic adsorption and photocatalytic degradation, membrane separation, sensing, and disinfection.[20–22] Although the MoS_2 band edge positions can be tuned to redox potentials that allow the generation of reactive oxygen species (ROS),[23,24] the photocatalytic performance of standalone MoS_2 nanosheets is compromised by its relatively low oxidation potential to amply produce hydroxyl radicals and the abundance of stable, though chemically inert, basal planes that reduce the number of active catalytic sites stemming primarily from edges and S vacancies.[25] Nanostructuring and heterojunction formation have been intensively pursued in order to alleviate these shortcomings by the deposition of MoS_2 nanosheets on nanostructured TiO_2 supports, including nanobelts,[26,27] nanotubes,[28,29] nanospheres,[30,31] facets,[32,33] and nanoparticles,[34,35] for the development of VLA MoS_2–TiO_2 photocatalysts. A prominent example has been provided by the vertically oriented growth of MoS_2 nanosheets on TiO_2 nanorods, leading to the preferential exposure of the highly reactive edge sites that also reduce electron and hole diffusion lengths, promoting charge separation and overall catalytic reaction rates.[36] Recently, surface modification of 2D TiO_2 nanohole arrays by dip coating in exfoliated MoS_2 nanosheet suspensions resulted in markedly improved photocatalytic activity,[37] while the incorporation of MoS_2 nanosheets in black TiO_2 microspheres for the formation of hierarchical tandem heterojunctions with CdS[38] and Cu_2S[39] nanoparticles resulted in highly efficient photocatalytic H_2 production assisted by photothermal effects.

In this work, heterostructured MoS_2–TiO_2 inverse opal films are demonstrated as efficient immobilized VLA photocatalysts for the degradation of pharmaceutical emerging contaminants, including two representative broad-spectrum antibiotics, tetracycline (TC) and ciprofloxacin (CIP), whose photocatalytic removal is attracting increasing attention toward water remediation.[40–44] The challenging integration of MoS_2 in three-dimensional (3D) TiO_2 PC films was undertaken via the co-assembly method, enabling the in situ incorporation of MoS_2 nanosheets to the TiO_2 inverse opal skeleton by a straightforward one-pot approach beyond conventional top-down (impregnation and spin/dip-coating) and bottom-up (chemical vapor, chemical bath, and hydrothermal) deposition methods. Structure–activity relations were explored for the MoS_2–TiO_2 PC films with respect to compositional and structural optimization as well as PBG engineering by varying

the nanosheet loading and colloidal template diameter together with performance screening on the VLA photocatalytic degradation of salicylic acid (SA), a persistent metabolite of acetylsalicylic acid that is commonly detected in wastewaters.[45] Low amounts of MoS_2 nanosheets in the nanocrystalline anatase walls of the PC films, which preserved the integrity of the periodic macroporous structure, resulted in a marked enhancement of the photocatalytic activity for pharmaceutical photodegradation under visible light, far beyond the performance of bare PC or benchmark P25 TiO_2 films. This improvement was related to the synergy of visible light trapping with the interfacial electron transfer between MoS_2 nanosheets and TiO_2 anatase nanoparticles in the nanocrystalline PC walls, as confirmed by electrochemical impedance and photoluminescence measurements.

2. MATERIALS AND METHODS

2.1. Chemicals and Reagents. Monodisperse polystyrene (PS) microspheres with mean diameters of 340, 425, and 460 nm and poly(methyl methacrylate) (PMMA) ones with 499 nm diameter (standard deviation SD = 10−11 nm) were purchased from microparticles GmbH in the form of colloidal dispersion of 5% solids (w/v) in DI water (2.7–3.0% CV). Titanium(IV) bis(ammonium lactato)dihydroxide (Ti-BALDH) 50 wt % aqueous solution, MoS_2 dispersion (1 mg/mL in H_2O, lateral size 50−1000 nm), and Hellmanex III were obtained from Sigma-Aldrich. All other reagents were of analytical or ACS reagent grade: ethanol (absolute, 99.8%), acetone (ACS reagent ≥99.5%), and hydrochloric acid (ACS reagent, fuming, ≥37%).

2.2. TiO_2 Inverse Opal Fabrication. Titania inverse opals were deposited by the convective evaporation-induced co-assembly of sacrificial polymer colloidal spheres of 340, 425, 460, and 499 nm mean diameters with the hydrolyzed TiBALDH sol−gel precursor.[46] This single-step process has been put forward as an effective method to evade conventional liquid phase infiltration into preassembled opal templates and improve the quality of inverse opal films.[47] In a typical deposition, cleaned (Hellmanex III, ultrasound acetone− EtOH) plain microscope or fluorine-doped tin oxide (FTO, thickness 2.2 mm, surface resistivity 7 Ω/sq) glass slides were nearly vertically suspended in a vial containing 10 mL of 0.125 wt % diluted polymer sphere suspension in Milli-Q water and 0.07 mL of fresh precursor (0.25 mL TiBALDH solution, 0.5 mL HCl 0.1 M, and 1 mL EtOH), both sonicated for 30 min before use. The vials were kept at 60 °C until the solvent fully evaporated, producing composite films that comprised titania gels within the polymer opal interstices. The dry films were calcined at 400 °C for 2 h in air (1 °C/min) to remove the colloidal template and crystallize the amorphous precursor in the inverse replica structure. The TiO_2 PC films were labeled as PC340, PC425, PC460, and PC499 after the diameter of the templating microspheres.

2.3. MoS_2–TiO_2 Inverse Opal Fabrication. In situ incorporation of MoS_2 nanosheets in the nanocrystalline walls of the TiO_2 inverse opals was implemented by the three-phase co-assembly technique, originally applied for the uniform incorporation of plasmonic nanoparticles in metal oxide PCs[48,49] and more recently for the fabrication of heterostructured WO_3/TiO_2 inverse opals.[50] This method was selected in order to facilitate the random orientation of MoS_2 nanosheet edges with respect to TiO_2 nanoparticles and the formation of firm interfaces (Scheme 1).
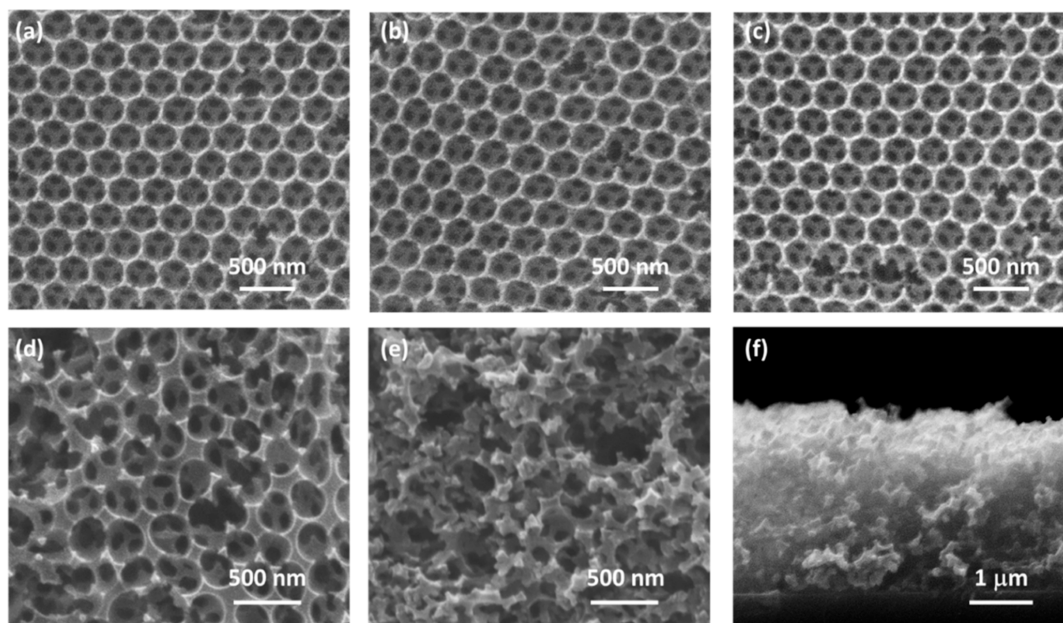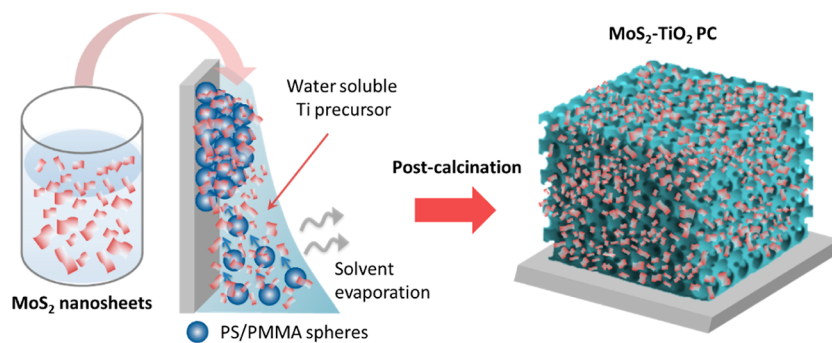
Scheme 1. Schematic Illustration of MoS$_2$–TiO$_2$ Inverse Opal Fabrication by Three Phase Co-assembly

Figure 1. SEM images for the TiO$_2$ PC425 films with increasing MoS$_2$ loading of (a) 0, (b) 0.1, (c) 0.3, (d) 0.4, and (e) 0.5 mL and (f) a cross-section image of 0.5 MoS$_2$-PC425.

Liquid cascade centrifugation was initially used for the size selection of MoS$_2$ nanosheets from the parent polydisperse MoS$_2$ suspension[51] in order to reduce its broad size distribution which proved detrimental for the inverse opal co-assembly. After probe sonication and centrifugation of the as-obtained dispersion at 1000 rpm, the supernatant was collected and subjected to successive centrifugations at increasing speeds in the range of 2000−8000 rpm, leading to a decrease in the concentration and average MoS$_2$ aggregate size. Small aliquots of the final MoS$_2$ dispersion obtained after 8000 rpm centrifugation (<0.01 mg/mL) were collected and redispersed at variable amounts in the suspension of the colloidal spheres and the TiBALDH precursor. Specifically, 0.1−0.6 mL of fresh MoS$_2$ dispersion replaced an equal part of Milli-Q water that was used to dilute the polymer sphere suspension to 0.125 wt %, followed by ultrasound sonication and mixing with 0.07 mL of fresh titania precursor, likewise bare TiO$_2$ inverse opals. Clean glass slides were nearly vertically suspended in vials containing 10 mL of the mixed colloid/titania/MoS$_2$ precursor and were kept at 60 °C until the solvent evaporated, leading to the assembly of MoS$_2$ nanosheets with the colloidal spheres and TiBALDH. The polymer template was subsequently removed by calcination at 400 °C for 2 h in air, leading to the inverse opal structure with

embedded MoS$_2$ nanosheets. The composite MoS$_2$–TiO$_2$ PC films were designated as 0.X MoS$_2$-PCYYY with 0.X being the volume (in mL) of the MoS$_2$ suspension and XXX being the diameter of the templating microspheres. Reference films were prepared by the immersion of PC films in the MoS$_2$ suspension, labeled as immersed PC films, as well as by spin coating a paste of the benchmark Aeroxide P25 mixed-phase titania nanocatalyst on glass slides followed by 400 °C calcination[52] in order to compare the MoS$_2$ loading on the photonic films and validate their photocatalytic performance on organic degradation, respectively.

2.4. Materials Characterization and Photocatalytic Evaluation. The PC films were characterized by scanning and transmission electron microscopies (SEM and TEM) together with energy-dispersive X-ray spectroscopy (EDX), X-ray and ultraviolet photoelectron spectroscopy (XPS-UPS), micro-Raman, photoluminescence (PL), as well as diffuse and specular reflectance UV−vis spectroscopies, and N$_2$ porosimetry, while electrochemical impedance spectroscopy (EIS) was carried out in a three-electrode configuration on PC films deposited on FTO substrates (Supporting Information, S1). The films' photocatalytic performance was evaluated on the degradation of SA, TC, and CIP pharmaceuticals under visible
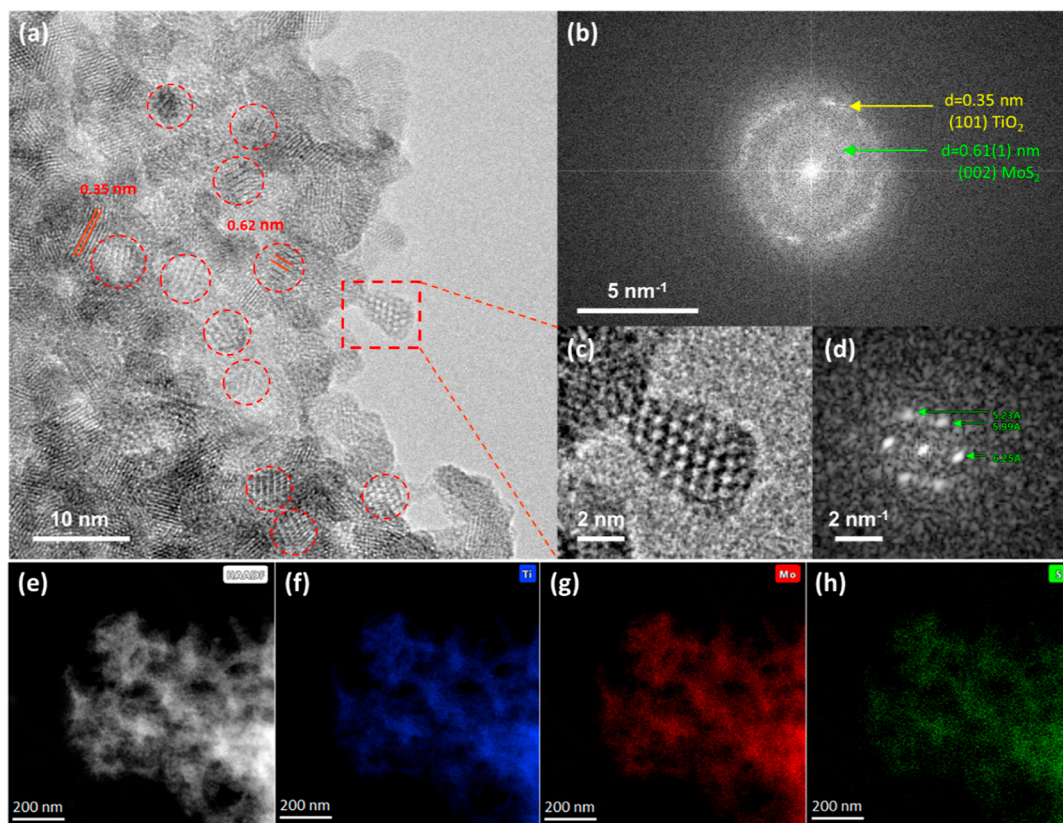
Figure 2. (a) TEM image of the nanocrystalline wall for 0.4 MoS2-PC425 and (b) corresponding FFT pattern. Red circles in (a) mark areas with (002) planes of 2H MoS$_2$ nanosheets among the characteristic (101) planes of the anatase nanoparticles. (c) Magnification of the TEM image depicting an isolated MoS$_2$ nanocrystallite at the wall edge and (d) the corresponding FFT pattern. (e) TEM image and the corresponding EDX maps for (f) Ti, (g) Mo, and (h) S elements.
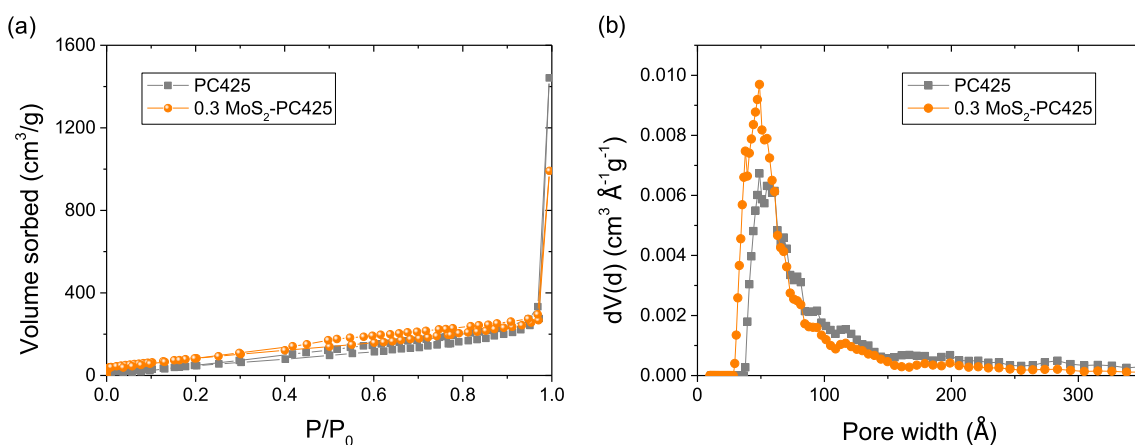

Figure 3. (a) Nitrogen adsorption−desorption isotherms for PC425 and 0.3 MoS$_2$-PC425 inverse opals and (b) the corresponding pore size distributions determined by the NLDFT equilibrium model (desorption branch).

light provided by a filtered Xe lamp source (Supporting Information, S2).

3. RESULTS AND DISCUSSION

3.1. Morphological and Structural Properties. Comparative SEM images of the pristine and final MoS$_2$ nanosheet dispersions centrifuged at 8000 rpm, drop-cast on Si substrates (Figure S1), indicated a decrease in the average lateral size of the MoS$_2$ nanosheets below about 120 nm. AFM measurements on MoS$_2$ films deposited by spin-coating the final (8000 rpm) dispersion on Si showed the formation of aggregates with

an average lateral size of 100−200 nm and average film roughness of 10 nm (Figure S2a), while TEM images of individual aggregates from the same dispersions identified the presence of ca. 10 layer MoS$_2$ slabs (Figure S2b). Optical measurements of the centrifuged MoS$_2$ dispersions at increasing speeds and after storage for a few days (Figure S3) showed a marked drop of absorbance after each centrifugation, reflecting the reduction of nanosheet concentration. The two characteristic exciton peaks A and B arising from the direct-gap transitions between the maxima of the MoS$_2$ split valence bands and the minimum of the conduction
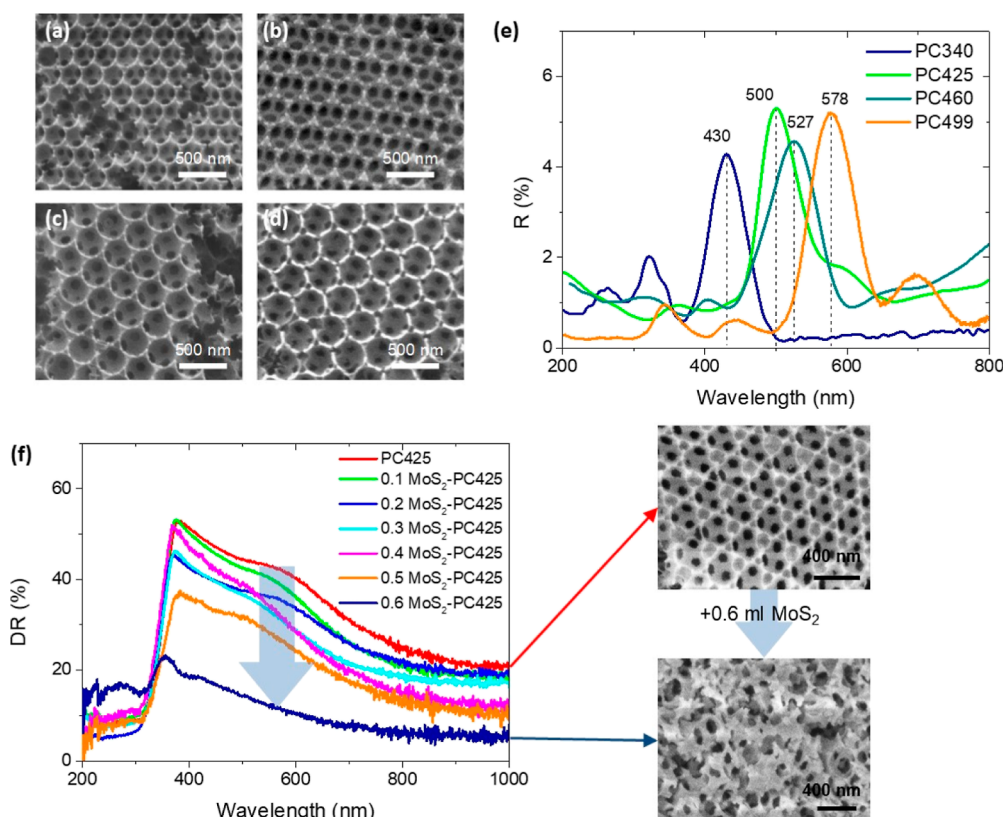
Figure 4. SEM images for the (a) PC340, (b) PC425, (c) PC460, and (d) PC499 inverse opal films and (e) the corresponding specular reflectance (R %) spectra at 15° incidence. (f) Diffuse reflectance (DR %) spectra for the MoS₂-PC425 films as a function of MoS₂ loading along with SEM images for the pristine PC425 and 0.6 MoS₂-PC425 films.

band at the K point of the Brillouin zone were clearly identified at 620 (2.0 eV) and 680 nm (1.82 eV) in the pristine MoS₂ dispersion.[16,17] The excitonic peaks blue-shifted to 605 and 664 nm, respectively, after 8000 rpm centrifugation, indicating the decrease of the average layer number,[51] while a weak re-entrant red-shift at 609 and 668 nm, respectively, was observed after 3 days' storage, indicative of aggregation effects.

Figure 1 shows representative SEM images for the co-assembled TiO₂ PC425 films with increasing volume loading of the final MoS₂ dispersion in the mixed colloid/TiBALDH precursor. Pristine PC425 displayed a well-ordered inverse opal structure corresponding to the (111) planes of an *fcc* lattice of 250 nm void macropores in place of the sacrificial colloidal spheres surrounded by a solid framework. The large macropores were interconnected through smaller ones at the contact points of adjacent PS spheres after calcination, which are essential for enhanced mass transport within the pore network. The addition of low amounts up to 0.3 mL of MoS₂ suspension in the complex precursor corresponds to about 1 Mo at % (Table S1) preserved intact in the periodic macropore structure (Figure 1b,c). However, the increase in the MoS₂ volume loading resulted in the progressive distortion of the inverse opal walls (Figure 1d) and the collapse of the periodic network to a disordered porous structure (Figure 1e,f).

The in situ incorporation and phase composition of MoS₂ nanosheets in the TiO₂ inverse opals were investigated by TEM and EDX elemental mapping, as shown in Figure 2. The formation of nanocrystalline walls consisting mainly of anatase crystallites with sizes below 10 nm was identified by the intense diffraction spots in the fast Fourier transform (FFT) patterns arising from the dominant (101) anatase planes with 0.35 nm

d-spacing (Figures 3b and S4). This is in agreement with previous results for the enhanced mesoporosity of co-assembled TiO₂ PC films using the TiBALDH precursor,[50] which retards the growth of anatase nanoparticles and the anatase−rutile phase transformation, maintaining the periodic inverse opal network that is essential for the development of highly efficient mesoporous anatase TiO₂ photocatalysts[7,8] accommodating heterojunctions with other VLA constituents.[38,39]

In addition, few-layer MoS₂ nanosheets oriented along different directions with respect to the anatase nanocrystallites were identified by the observation of the hexagonal (002) planes of the 2H MoS₂ phase with ca. 0.62 nm *d*-spacing (Figure 2a), confirming their incorporation in the TiO₂ inverse opal skeleton. The FFT pattern of an isolated MoS₂ nanocrystallite protruding from the inverse opal wall (Figure 2c) showed diffraction spots of variable spacing around 0.61(1) nm (Figure 2d), leading to the diffuse diffraction ring in the FFT pattern (Figure 3b) derived for the whole TEM image. This indicates that the formation of structural defects in the embedded MoS₂ nanosheets is most likely due to sulfur vacancies,[53] complying with the deviations of Mo/S stoichiometry from the ideal 1:2 ratio detected by EDX (Table S1). Moreover, EDX mapping (Figure 2e−h) showed a uniform distribution of Mo and S species with respect to Ti throughout the skeleton of the composite structure comprising MoS₂−TiO₂ interfaces with diverse orientations.

The structural and compositional properties of MoS₂−TiO₂ PCs were investigated by Raman spectroscopy. The Raman spectra of both 0.4 MoS₂-PC425 and pristine PC425 films exhibited the characteristic Raman-active modes of anatase
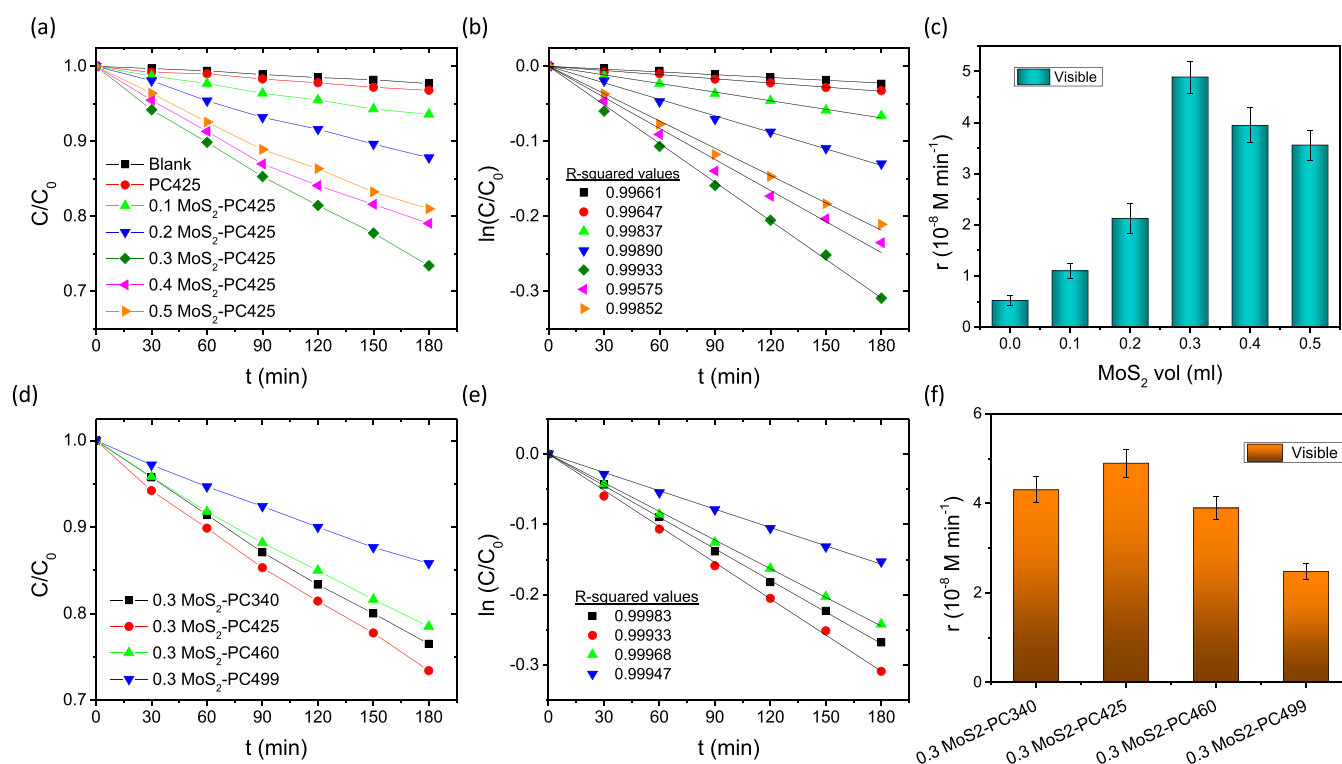
Figure 5. SA photodegradation kinetics and the corresponding reaction rates r under visible light as a function of (a−c) the MoS_2 loading amount for the MoS_2-PC425 films and (d−f) the macropore diameters of the 0.3 MoS_2-PC425 films.

TiO2 at ca. 148 (E_g), 199 (E_g), 399 (B_{1g}), 518 (A_{1g} + B_{1g}), and 641 cm^{-1} (E_g), as shown in Figure S5a. The observed shifts and broadening of the Raman bands with respect to bulk anatase can be related to the growth of anatase nanoparticles with a size below 10 nm in TiO2 PCs using TiBALDH,[46] which leads to the breakdown of the q = 0 selection rule for Raman scattering.[54] In addition, weak shoulders were traced at about 382 and 406 cm^{-1} for 0.4 MoS_2-PC425, corresponding closely to the two characteristic optical phonons of 2H−MoS_2 arising from the opposite, the in-plane vibrations of S atoms relative to Mo and the out-of-plane vibrations of S atoms, respectively.[55] The latter modes were clearly identified for MoS_2 suspensions drop-cast on glass as well as for the immersed MoS_2-PC425 films (Figure S5a).

The chemical composition of the MoS_2−TiO2 inverse opals was traced by XPS. The Ti $2p_{3/2}$ and $2p_{1/2}$ doublets could be accurately fit with two peaks at 458.4 and 464.1 eV, respectively, with spin−orbit splitting of 5.7 eV, for all TiO2 PC films (Figure S5b), confirming the presence of Ti^{4+} ions and stoichiometric anatase TiO2.[56] However, the presence of MoS_2 nanosheets was identified only for the immersed MoS_2-PC425 films in the corresponding Mo 3d (Figure S5c) and S 2p (Figure S5d) core-level spectra. In the former case, Mo 3d spectrum deconvolution revealed a major contribution from a doublet at binding energies of 228.9 and 232.1 eV (spin−orbit splitting of 3.2 eV) corresponding to the Mo $3d_{5/2}$ and $3d_{3/2}$ peaks of Mo^{4+} ions in MoS_2,[57] while a minor contribution was derived at 231.9 and 235.1 eV, indicating Mo^{6+} ions, most likely arising from oxidation of the initial suspension during storage in ambient atmosphere.[29] The presence of S^{2-} was confirmed by the S 2s signal at 225.9 eV (Figure S5c) and the S 2p doublet (Figure S5c), which was deconvoluted with two distinct $2p_{3/2}$ and $2p_{1/2}$ peaks at binding energies of 161.9 and 163 eV, respectively.[57] However, only a rather weak Mo 3d

signal could be traced at about 229.1 eV for the 0.3 MoS_2-PC425 film, reflecting the low amount of MoS_2 nanosheets incorporated into the TiO2 inverse opals.

The textural properties were comparatively investigated by N2 porosimetry for the unmodified PC425 and 0.3 MoS_2-PC425 inverse opals (Figure 3). The high surface area reaching 244 m^2/g was estimated by applying the multipoint Brunauer−Emmett−Teller (BET) method to the pristine PC425 that originated from the enhanced mesoporosity of the nanocrystalline inverse opal skeleton. This was further corroborated by the corresponding pore size distribution determined from nonlocal density functional theory (NLDFT) analysis using the N2−silica desorption branch kernel (equilibrium model) at 77 K (Figure 3b).[58] Markedly increased mesopore volume (V_{meso}) of 0.499 cm^3/g was thus derived by the NLDFT pore size distribution with a maximum at 4.89 nm mesopore width, which can be related to the small anatase nanoparticle size.[46] Further improvement of surface area that reached 347 m^2/g was derived for 0.3 MoS_2-PC425, while the mesopore volume showed a relatively small decrease to 0.444 cm^3/g indicating that the integration of the relatively bulkier MoS_2 nanosheets in the nanocrystalline anatase walls mainly affected the inverse opal macroporosity compared to the mesopore distribution.

3.2. Optical Properties. PBG tuning in the TiO2 photonic films was monitored by specular reflectance (R %) at a 15° angle of incidence as a function of the inverse opal macropore size (Figure 4a−e). A clear R % peak due to Bragg reflection was invariably observed for all PC films, verifying the formation of the incomplete PBG (stop band) along the [111] direction in the inverse opal structure.[12] The stop band positions red-shifted with increasing void diameter (D) (Table S2), following the increase in the templating microsphere size. The R % peak positions were analyzed by applying the modified Bragg law for first-order diffraction from the (111) *fcc*
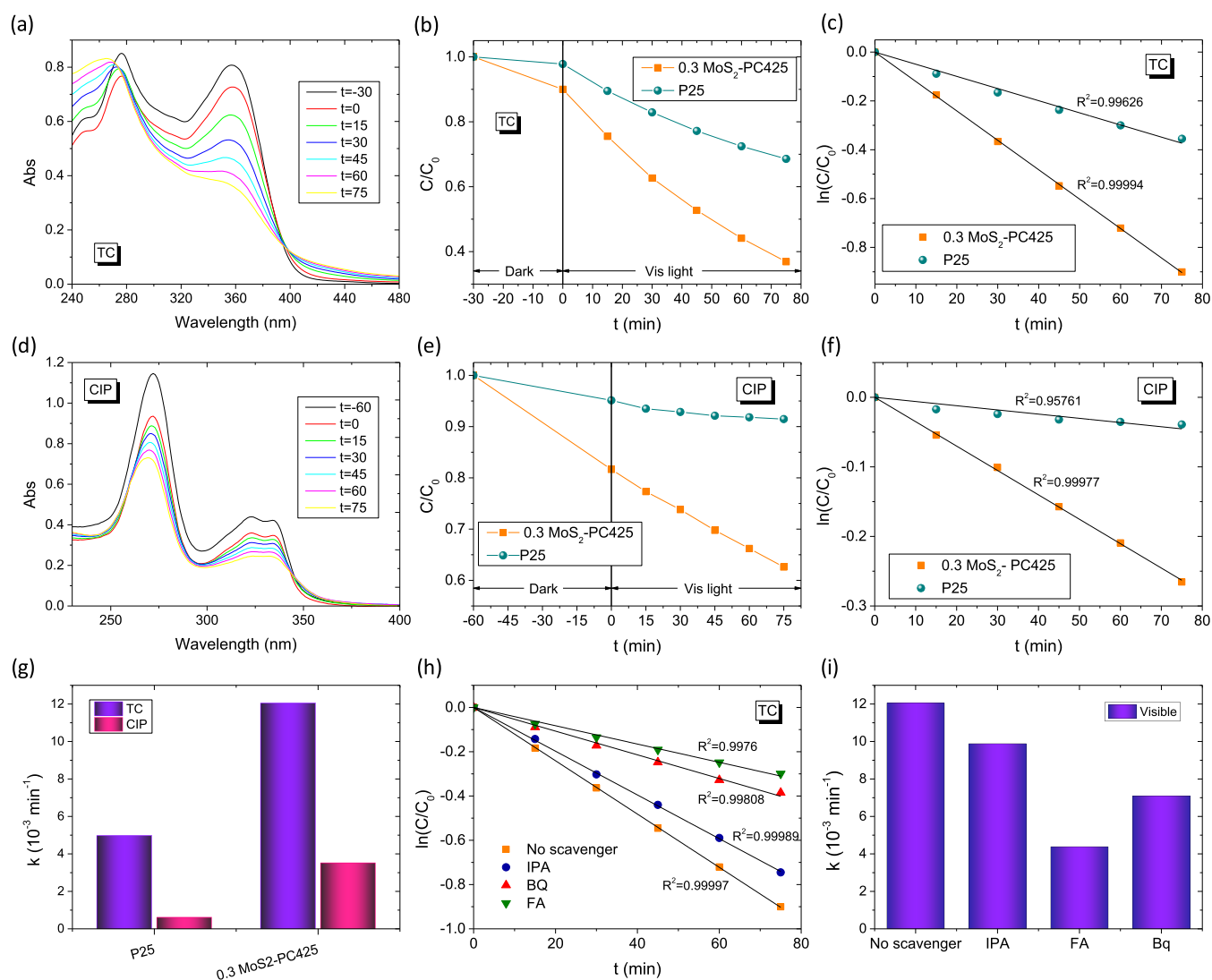
Figure 6. (a−c) TC and (d−f) CIP absorbance spectra in the presence of 0.3 MoS$_2$-PC425 films and photodegradation kinetics. (g) Apparent kinetic constants k for TC and CIP degradation under visible light. (h) TC photodegradation in the presence of IPA, FA, and Bq radical scavengers and (i) the corresponding apparent kinetic constants k variation.

planes (Supporting Information, S1). Using the observed wavelengths at $\theta = 15°$ and the measured diameters D, the effective refractive index n_{eff} values and filling fractions $(1 - f)$ were determined in air for $n_{TiO_2} = 2.55$ and $n_{air} = 1.0$ (Table S2). The obtained $1 - f$ values were appreciably smaller than the theoretical one of 0.26 for complete filling of the inverse *fcc* lattice, reflecting the enhanced mesoporosity of the nanocrystalline anatase skeletal walls in the co-assembled films.[46] The derived filling fractions were then used to estimate the stop band positions in water $((n_{H_2O}) = 1.33)$, where the photocatalytic reaction takes place (Table S2).

The effect of MoS$_2$ loading on the optical response and photonic properties of the MoS$_2$−TiO$_2$ inverse opals was explored by diffuse reflectance (DR %) measurements for PC films of constant void diameter, namely, the MoS$_2$-PC425 (Figure 4f). An intense, broad DR % band was observed for pristine PC425 at about 550 nm, clearly separated from the anatase absorption edge at 375 nm. Both the DR % intensity and width were considerably higher than those of the R % spectra, reflecting the presence of different PC domains within the area probed by the coarse focused beam (spot size of ca. 2

mm^2). The DR % intensity decreased gradually with the increase of MoS$_2$ loading until it was completely suppressed for 0.6 MoS$_2$-PC425. This variation can be associated with the increase in broadband electronic absorbance from the MoS$_2$ nanosheets together with the distortion of the inverse opal structure, as evidenced by comparative SEM images for PC425 and 0.6 MoS$_2$-PC425 films (Figure 4f).

3.3. Photocatalytic Performance vs Composition and Light Trapping. Photocatalytic activity screening of the MoS$_2$−TiO$_2$ PC films was performed using SA as a model pollutant under visible light at pH = 3 (Figure 5), where direct oxidation by valence band holes takes place.[59] SA is a colorless pharmaceutical water contaminant that, unlike dyes, absorbs well below the PC film stop bands in the visible range (Figure S6a) and thus precludes any slow photon contribution via spectral overlap with the molecular electronic absorption. Blank experiments in the absence of photocatalytic films as well as in the presence of unmodified PC425 films showed negligible SA degradation under visible light (Figure 5a). On the other hand, visible light illumination in the presence of MoS$_2$-PC425 films, after dark adsorption, resulted in a

continuous decrease of SA concentration (C) with time, which was determined spectrophotometrically by the characteristic SA absorption band at 300 nm (Figure S6a). The $\ln(C/C_0)$ vs t plot, where C_0 is the initial SA concentration after dark adsorption, varied linearly with time (Figure 5b, e), indicating that SA photodegradation followed pseudo-first-order kinetics. The apparent kinetic constants k were determined from the slopes of the linear $\ln(C/C_0)$ vs t plots (Figure S6b,c), and the corresponding reaction rates were then calculated as $r = kC_0$ for low (<mM) pollutant concentrations in order to determine the films' activity, independently of C_0 variations due to SA adsorption.

The derived r values presented nonmonotonous variation with the MoS_2 loading (Figure 5c), despite the continuous rise of visible light absorbance in the optical spectra of the MoS_2-PC425 films (Figure 4f). The highest rate was observed for 0.3 MoS_2-PC425 films, indicating that maintaining the integrity of the periodic inverse opal structure in combination with visible light harvesting provided by MoS_2 nanosheets are key factors for the photocatalytic performance of MoS_2-PC425 films.

To explore light trapping by the MoS_2-TiO_2 PC films, SA photocatalytic tests were carried out as a function of the inverse opal diameter for the optimal 0.3 MoS_2 loading (Figure 5d,e). The obtained rates varied considerably with the macropore size, indicating significant differences in the light-harvesting ability for the 0.3 MoS_2-PC films (Figure 5f). Specifically, 0.3 MoS_2-PC425 presented the highest r value, followed closely by 0.3 MoS_2-PC340, whereas the larger diameter inverse opals showed successively lower activities, reaching approximately a 2-fold drop for 0.3 MoS_2-PC499. This size-selective performance indicates that stop band tuning close to the MoS_2 excitonic peaks results in optimal light trapping for 0.3 MoS_2-PC425, whose PBG is expected at about 610 nm in water (Table S2). Assuming that the PBG spectral width is about the full width at half-maximum of the R % peak of ≈60 nm (Figure 4e), the stop band in water will extend in the range of 610 ± 30 nm between the A and B exciton bands. The corresponding red- and blue-edge slow photons,[60,61] which span a narrower spectral range of about 20–30 nm, can be predicted to occur roughly above 640 nm and below 580 nm, respectively, extending over an appreciably broad spectral range of weak electronic absorbance due to the low amount of MoS_2 nanosheets. A red-shift of the light trapping range by about 40 nm can be expected for 0.3 MoS_2-PC460 (Table S2), whose PBG is estimated at 650 ± 30 nm, leading to a relatively smaller spectral overlap with the MoS_2 excitonic transitions. Improved light trapping is also inferred for the smaller diameter 0.3 MoS_2-PC340 films, whose PBG edges in water (<480 and >540 nm) overlap with the higher energy absorbance of the MoS_2 nanosheets (Figure S3). On the other hand, no appreciable photonic effects are expected for the larger diameter PC499 films, whose stop band in water occurs well above 700 nm, where MoS_2 is not expected to show any appreciable electronic absorbance.

3.4. Antibiotics Photocatalytic Degradation. The best-performing 0.3 MoS_2-PC425 films were subsequently selected for advanced application in the VLA photocatalytic degradation of TC and CIP as representatives of tetracycline and quinolone antibiotics, whose residues and metabolites in wastewaters are a major environmental hazard to human health.[62] Blank experiments showed negligible degradation for both TC and CIP antibiotics under visible light, whose concentrations were spectrophotometrically determined by the

corresponding absorbance bands at 357 nm (Figure 6a) and 277 nm (Figure 6d). Relatively slow TC and CIP degradation kinetics were observed, following dark adsorption, in the presence of mesoporous TiO_2 reference films deposited using a paste of the benchmark anatase−rutile P25 nanocatalyst (Figure S7), which has been recently shown to degrade TC under visible light by means of the sensitization mechanism.[40] On the other hand, the presence of 0.3 MoS_2-PC425 films resulted in markedly enhanced VLA reduction of TC and CIP concentrations reaching degradation levels, defined as $(1 − C/C_0) \times 100\%$ of 56% (Figure 6b) and 23% (Figure 6e), respectively, after 60 min of visible light illumination. Both TC and CIP photodegradation kinetics followed pseudo-first-order kinetics (Figure 6c,f), with apparent kinetic constants k of 0.0119 and 0.00351 min^{-1}, respectively, which are comparable to those reported for TC and CIP photodegradation by MoS_2-TiO_2[43,63] as well as other heterostructured photocatalysts involving MoS_2 and Bi-based and carbon nitride VLA semiconductors in the form of powders (Table S3). The photocatalytic stability of the 0.3 MoS_2-PC425 films was assessed after four successive TC degradation experiments under visible light using the same film, where a small decrease in photocatalytic activity (the kinetic constants k decreased by ca. 6%) was observed (Figure S8). Moreover, TEM images and the corresponding EDX elemental maps for the 0.3 MoS_2-PC425 films after TC photocatalytic tests confirmed the uniform coverage of the TiO_2 inverse opal walls with MoS_2 nanosheets (Figure S9a−d). The latter could be directly identified in the local FFT pattern of TEM images for the used films by the characteristic 0.61 nm d-spacing of the (002) planes of the 2H MoS_2 phase (Figure S9e), corroborating the strong MoS_2-TiO_2 interfacial coupling. The obtained results are very promising considering the immobilized state of MoS_2-PCs that avoids catalyst recovery and separation issues, as well as the much lower catalyst loading compared to powder photocatalysts mainly applied for TC and CP degradation.[64]

In order to investigate ROS generation and the mechanism underlying antibiotic photodegradation by MoS_2-TiO_2 PC films under visible light, photocatalytic experiments were carried out in the presence of 5 mM isopropanol (IPA), formic acid (FA), and 1 mM 1,4 benzoquinone (Bq) as hydroxyl (•OH), hole (h^+), and superoxide (•O_2^-) radical scavengers, respectively (Figure 6h). IPA addition had a relatively weak, detrimental effect on TC degradation, which was drastically inhibited by the presence of Bq (40% reduction of k) and mainly FA (63% reduction of k), indicating that h^+ and •O_2^- radicals are the major ROS involved in TC degradation by MoS_2-TiO_2 PCs under visible light, whereas •OH radicals play a minor role. Furthermore, in order to validate the performance of the optimal photocatalyst, TC degradation was also monitored by high-performance liquid chromatography (HPLC) for the 0.3 MoS_2-PC425 photonic films under visible and UV−vis light for 3 h (Supporting Information, S2). The obtained results showed high TC degradation levels that reached 93 and 99% after 2 h of visible and UV−vis light irradiation, respectively (Figure S10), supporting the excellent VLA photocatalytic activity of the optimized MoS_2-TiO_2 PC films.

3.5. Charge Separation. To investigate charge separation in the MoS_2-PC films, EIS measurements were carried out on the best-performing 0.3 MoS_2-PC425 with respect to PC425 films, deposited on FTO substrates under dark and visible light irradiation. Comparative Nyquist plots showed that the radius
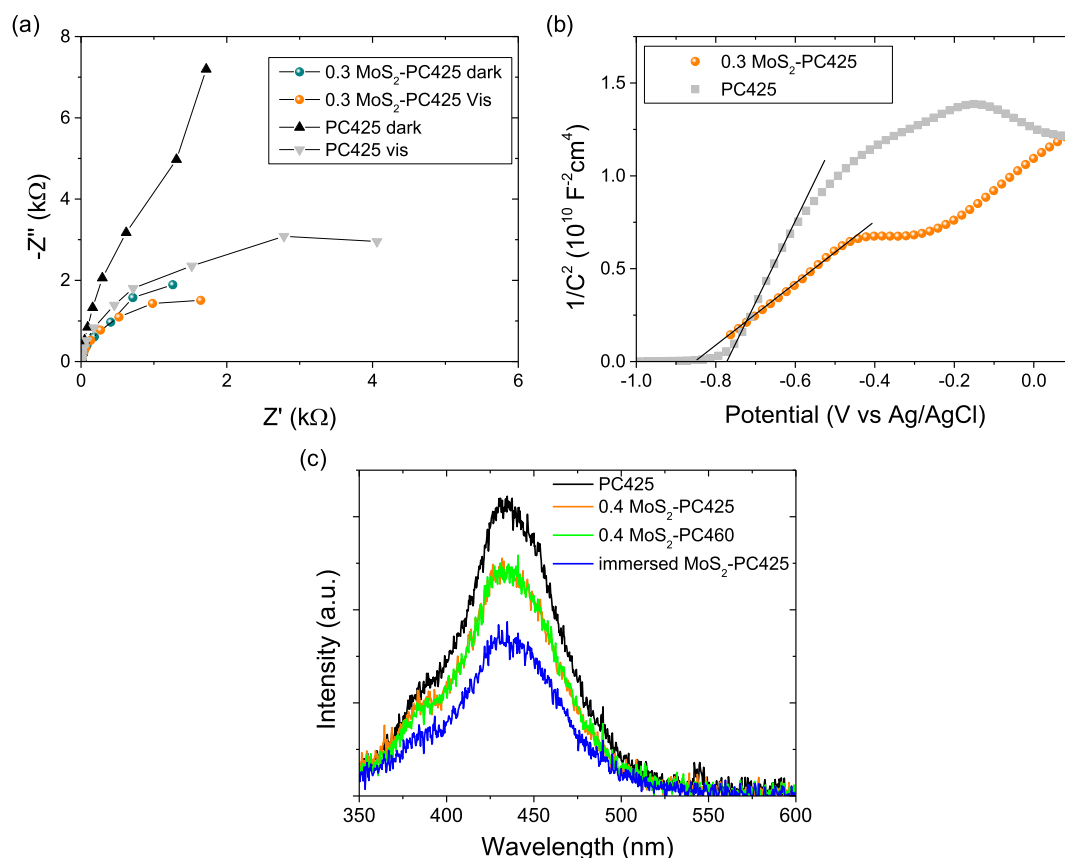
Figure 7. (a) EIS Nyquist, (b) Mott−Schottky plots for 0.3 MoS₂-PC425 and PC425 photoelectrodes under visible light, and (c) PL spectra of MoS₂−TiO₂ PC425 films compared to pristine PC425.

of the capacitive arc at higher frequencies in the EIS plane decreased for 0.3 MoS$_2$-PC425 compared to the pristine PC425 films under both dark and visible light conditions (Figure 7a), indicative of a reduced charge transfer resistance in the composite films. The flatband potential and donor densities in the 0.3 MoS$_2$-PC425 and PC425 photoelectrodes were derived by measuring the capacitance C of the semiconductor/electrolyte junction as a function of the applied potential and the corresponding Mott−Schottky plots (Figure 7b), i.e., the variation of $1/C^2$ vs applied potential, using the following relation

$$\frac{1}{C^2} = \frac{2}{eA^2\varepsilon\varepsilon_0 N_D}\left(V - V_{fb} - \frac{kT}{e}\right)$$

where e is the elementary charge, A is the surface area of the electrode, N_D is the donor density, ε is the permittivity of the semiconductor electrode, ε_0 is the vacuum permittivity, V_{fb} is the flatband potential, T is the absolute temperature, and k is Boltzman's constant.

The V_{fb} values determined from the corresponding x-intercepts of the best linear regression curves on the corresponding Mott−Schottky plots presented a negative shift from −0.77 V for PC425 to −0.87 V vs Ag/AgCl for 0.3 MoS$_2$-PC425. In addition, the donor density N_D derived from the slopes of the best-fit linear curves was enhanced from 3.3×10^{19} cm^{-3} for PC425 to 8.3×10^{19} cm^{-3} for 0.3 MoS$_2$-PC425. The size-dependent conduction band of MoS$_2$ nanosheets is expected to shift toward more negative redox potentials,[23,24,37] allowing visible-light-induced charge transfer between MoS$_2$ and TiO$_2$ and facilitating the generation of

superoxide radicals, which are the major ROS in TC degradation. The enhanced charge separation was further supported by PL measurements under 275 nm excitation (Figure 7c). The PL spectrum of pristine PC425 showed a weak emission band at ca. 385 nm along with a stronger peak at ca. 430 nm related to the near-band gap emission and shallow defect states for anatase nanoparticles.[50] The incorporation of MoS$_2$ nanosheets in the TiO$_2$ PCs caused a significant decrease of PL intensity, corroborating the presence of strong MoS$_2$−TiO$_2$ interfacial coupling that reduces electron−hole recombination. Considering the broad size distribution of MoS$_2$ nanosheets and their random orientation relative to the anatase nanoparticles, the formation of diverse MoS$_2$−TiO$_2$ heterojunctions in the inverse opal skeleton can be accordingly concluded, which promotes MoS$_2$−TiO$_2$ charge separation and ROS generation for pharmaceutical degradation.

4. CONCLUSIONS

In summary, heterostructured MoS$_2$−TiO$_2$ inverse opal photocatalysts were fabricated by the three-phase convective evaporation-induced co-assembly of sacrificial colloidal spheres with a water-soluble Ti precursor and an aqueous dispersion of MoS$_2$ nanosheets, which enabled their integration into the nanocrystalline TiO$_2$ inverse opal skeletal walls by a facile, one-pot method. Liquid cascade centrifugation was applied to narrow down the polydispersity of MoS$_2$ nanosheets, which were incorporated at variable loading amounts in the co-assembly mixture in combination with polymer-templating microspheres of different diameters. This allowed composi-

tional and PBG engineering of the MoS_2–TiO_2 PC films, whose optimization was carried out by performance screening on SA photocatalytic degradation under visible light. The incorporation of low amounts of MoS_2 nanosheets in the inverse opal framework preserved the integrity and photonic properties of the periodic macroporous structure while enhancing the available surface area, leading to highly efficient photocatalytic films validated on the VLA degradation of TC and CIP broad-spectrum antibiotics, far beyond the performance of bare PC or benchmark P25 TiO_2 films. The combination of broadband MoS_2 visible light absorption and photonic-assisted light trapping together with enhanced charge separation and ROS formation stemming from the intimate assembly between MoS_2 nanosheets and TiO_2 nanoparticles in the inverse opal walls, is concluded as a promising approach to fabricating efficient immobilized PC photocatalysts for the degradation of pharmaceutical emerging contaminants in water.

■ ASSOCIATED CONTENT

Ⓢ Supporting Information

The Supporting Information is available free of charge at https://pubs.acs.org/doi/10.1021/acsomega.3c03881.

> SEM images for MoS_2 dispersions on Si substrates; AFM and TEM images of MoS_2 nanosheets; absorbance spectra for MoS_2 dispersions at different centrifugation speeds; TEM analysis for 0.3 MoS_2-PC460; Raman and XP spectra for MoS_2-PC and reference films; SA absorbance spectra and apparent kinetic constant variation under visible light; top-view and cross-section SEM images of P25 reference films; stability tests on TC photodegradation under visible light; elemental EDX maps and TEM analysis for 0.3 MoS_2-PC425 films after TC photocatalysis; TC degradation monitored by HPLC in the presence of 0.3 MoS_2-PC425 films under visible and UV–vis light irradiation; EDX analysis for the TiO_2 PC425 films with different MoS_2 volume loadings; structural and optical parameters for the TiO_2 PC films; and performance comparison on TC and CIP photodegradation by heterostructured MoS_2 photocatalysts under visible light (PDF)

■ AUTHOR INFORMATION

Corresponding Author

Vlassis Likodimos − *Section of Condensed Matter Physics, Department of Physics, National and Kapodistrian University of Athens, Athens 15784, Greece;* ⓘ orcid.org/0000-0002-0102-769X; Email: vlikodimos@phys.uoa.gr

Authors

Stelios Loukopoulos − *Section of Condensed Matter Physics, Department of Physics, National and Kapodistrian University of Athens, Athens 15784, Greece*

Elias Sakellis − *Institute of Nanoscience and Nanotechnology, National Center for Scientific Research "Demokritos", Athens 15341, Greece*

Marios G. Kostakis − *Laboratory of Analytical Chemistry, Department of Chemistry, National and Kapodistrian University of Athens, Athens 15771, Greece;* ⓘ orcid.org/0000-0001-7775-4634

Dimitrios-Triantafyllos Gerokonstantis − *Laboratory of Analytical Chemistry, Department of Chemistry, National and Kapodistrian University of Athens, Athens 15771, Greece*

Polychronis Tsipas − *Institute of Nanoscience and Nanotechnology, National Center for Scientific Research "Demokritos", Athens 15341, Greece;* ⓘ orcid.org/0000-0001-9064-9601

Spiros Gardelis − *Section of Condensed Matter Physics, Department of Physics, National and Kapodistrian University of Athens, Athens 15784, Greece;* ⓘ orcid.org/0000-0001-8340-8025

Athanassios G. Kontos − *Institute of Nanoscience and Nanotechnology, National Center for Scientific Research "Demokritos", Athens 15341, Greece; Department of Physics, School of Applied Mathematical and Physical Sciences, National Technical University of Athens, Athens 15780, Greece;* ⓘ orcid.org/0000-0001-9193-0198

Fotis K. Katsaros − *Institute of Nanoscience and Nanotechnology, National Center for Scientific Research "Demokritos", Athens 15341, Greece*

Zili Sideratou − *Institute of Nanoscience and Nanotechnology, National Center for Scientific Research "Demokritos", Athens 15341, Greece*

George Em. Romanos − *Institute of Nanoscience and Nanotechnology, National Center for Scientific Research "Demokritos", Athens 15341, Greece*

Athanasios Dimoulas − *Institute of Nanoscience and Nanotechnology, National Center for Scientific Research "Demokritos", Athens 15341, Greece;* ⓘ orcid.org/0000-0003-3199-1356

Nikolaos S. Thomaidis − *Laboratory of Analytical Chemistry, Department of Chemistry, National and Kapodistrian University of Athens, Athens 15771, Greece;* ⓘ orcid.org/0000-0002-4624-4735

Complete contact information is available at:
https://pubs.acs.org/10.1021/acsomega.3c03881

Author Contributions

The manuscript was written through the contributions of all authors. All authors have given their approval to the final version of the manuscript.

Notes

The authors declare no competing financial interest.

■ ACKNOWLEDGMENTS

■ REFERENCES

(1) Schneider, J.; Matsuoka, M.; Takeuchi, M.; Zhang, J.; Horiuchi, Y.; Anpo, M.; Bahnemann, D. W. Understanding TiO_2 Photocatalysis: Mechanisms and Materials. *Chem. Rev.* **2014**, *114*, 9919−9986.

(2) Li, Z.; Wang, S.; Wu, J.; Zhou, W. Recent Progress in Defective TiO_2 Photocatalysts for Energy and Environmental Applications. *Renewable Sustainable Energy Rev.* **2022**, *156*, 111980.

(3) Feizpoor, S.; Rahim Pouran, S.; Habibi-Yangjeh, A. Recent Progress on Photocatalytic Evolution of Hydrogen Gas over TiO_{2-x}-based Emerging Nanostructures. *Mater. Sci. Semicond. Process.* **2023**, *162*, 107444.

(4) Akhundi, A.; Badiei, A.; Ziarani, G. M.; Habibi-Yangjeh, A.; Muñoz-Batista, M. J.; Luque, R. Graphitic Carbon Nitride-Based Photocatalysts: Toward Efficient Organic Transformation for Value-Added Chemicals Production. *Mol. Catal.* **2020**, *488*, 110902.

(5) Akhundi, A.; Zaker Moshfegh, A.; Habibi-Yangjeh, A.; Sillanpää, M. Simultaneous dual-functional photocatalysis by g-C_3N_4-based nanostructures. *ACS ES&T Engg* **2022**, *2*, 564−585.

(6) Sabri, M.; Habibi-Yangjeh, A.; Rahim Pouran, S.; Wang, C. Titania-Activated Persulfate for Environmental Remediation: The-State-of-the-Art. *Catal. Rev.* **2023**, *65*, 118−173.

(7) Zhou, W.; Sun, F.; Pan, K.; Tian, G.; Jiang, B.; Ren, Z.; Tian, C.; Fu, H. Well-Ordered Large-Pore Mesoporous Anatase TiO_2 with Remarkably High Thermal Stability and Improved Crystallinity: Preparation, Characterization, and Photocatalytic Performance. *Adv. Funct. Mater.* **2011**, *21*, 1922−1930.

(8) Zhou, W.; Li, W.; Wang, J.-Q.; Qu, Y.; Yang, Y.; Xie, Y.; Zhang, K.; Wang, L.; Fu, H.; Zhao, D. Ordered Mesoporous Black TiO_2 as Highly Efficient Hydrogen Evolution Photocatalyst. *J. Am. Chem. Soc.* **2014**, *136*, 9280−9283.

(9) Liu, J.; Zhao, H.; Wu, M.; Van der Schueren, B.; Li, Y.; Deparis, O.; Ye, J.; Ozin, G. A.; Hasan, T.; Su, B. L. Slow Photons for Photocatalysis and Photovoltaics. *Adv. Mater.* **2017**, *29*, 1605349.

(10) Beydoun, N.; Farhat, R.; Halaoui, L. I. Enhanced Solar Light Harvesting with Q-CdTe/Se Sensitized Inverse Opal TiO_2. *ACS Appl. Energy Mater.* **2020**, *3*, 3104−3119.

(11) Madanu, T. L.; Mouchet, S. R.; Deparis, O.; Liu, J.; Li, Y.; Su, B.-L. Tuning and Transferring Slow Photons from TiO_2 Photonic Crystals to $BiVO_4$ Nanoparticles for Unprecedented Visible Light Photocatalysis. *J. Colloid Interface Sci.* **2023**, *634*, 290−299.

(12) Likodimos, V. Photonic Crystal-assisted Visible Light Activated TiO_2 Photocatalysis. *Appl. Catal., B* **2018**, *230*, 269−303.

(13) Singh, A. K.; Kumar, P.; Late, D.; Kumar, A.; Patel, S.; Singh, J. 2D Layered Transition Metal Dichalcogenides (MoS_2): Synthesis, Applications and Theoretical Aspects. *Appl. Mater. Today* **2018**, *13*, 242−270.

(14) Chen, B.; Meng, Y.; Sha, J.; Zhong, C.; Hu, W.; Zhao, N. Preparation of MoS_2/TiO_2 Based Nanocomposites for Photocatalysis and Rechargeable Batteries: Progress, Challenges and Perspective. *Nanoscale* **2018**, *10*, 34−68.

(15) Wang, J.; Fu, K.; Zhang, X.; Yin, Q.; Wei, G.; Su, Z. When MoS_2 Meets TiO_2: Facile Synthesis Strategies, Hybrid Nanostructures, Synergistic Properties, and Photocatalytic Applications. *J. Mater. Chem. C* **2021**, *9*, 8466−8482.

(16) Mak, K. F.; Lee, C.; Hone, J.; Shan, J.; Heinz, T. F. Atomically Thin MoS_2: A New Direct-Gap Semiconductor. *Phys. Rev. Lett.* **2010**, *105*, 136805.

(17) Splendiani, A.; Sun, L.; Zhang, Y.; Li, T.; Kim, J.; Chim, C.-Y.; Galli, G.; Wang, F. Emerging Photoluminescence in MoS_2. *Nano Lett.* **2010**, *10*, 1271−1275.

(18) Bhimanapati, G. R.; Lin, Z.; Meunier, V.; Jung, Y.; Cha, J.; Das, S.; Xiao, D.; Son, Y.; Strano, M. S.; Cooper, V. R.; Liang, L.; Louie, S. G.; Ringe, E.; Zhou, W.; Kim, S. S.; Naik, R. R.; Sumpter, B. G.; Terrones, H.; Xia, F.; Wang, Y.; Zhu, J.; Akinwande, D.; Alem, N.; Schuller, J. A.; Schaak, R. E.; Terrones, M.; Robinson, J. A. Recent Advances in Two-Dimensional Materials Beyond Graphene. *ACS Nano* **2015**, *9*, 11509−11539.

(19) Lu, Q.; Yu, Y.; Ma, Q.; Chen, B.; Zhang, H. 2D Transition-Metal-Dichalcogenide-Nanosheet-Based Composites for Photocatalytic and Electrocatalytic Hydrogen Evolution Reactions. *Adv. Mater.* **2016**, *28*, 1917−1933.

(20) Wang, Z.; Mi, B. Environmental Applications of 2D Molybdenum Disulfide (MoS_2) Nanosheets. *Environ. Sci. Technol.* **2017**, *51*, 8229−8244.

(21) Li, Z.; Meng, X.; Zhang, Z. Recent Development on MoS_2-based Photocatalysis: A Review. *J. Photochem. Photobiol., C* **2018**, *35*, 39−55.

(22) Hasija, V.; Raizada, P.; Thakur, V. K.; Parwaz Khan, A. A.; Asiri, A. M.; Singh, P. An Overview of Strategies for Enhancement in Photocatalytic Oxidative Ability of MoS_2 for Water Purification. *J. Environ. Chem. Eng.* **2020**, *8*, 104307.

(23) Thurston, T.; Wilcoxon, J. Photooxidation of Organic Chemicals Catalyzed by Nanoscale MoS_2. *J. Phys. Chem. B* **1999**, *103*, 11−17.

(24) Liu, C.; Kong, D.; Hsu, P.-C.; Yuan, H.; Lee, H.-W.; Liu, Y.; Wang, H.; Wang, S.; Yan, K.; Lin, D.; Maraccini, P. A.; Parker, K. M.; Boehm, A. B.; Cui, Y. Rapid Water Disinfection Using Vertically Aligned MoS_2 Nanofilms and Visible Lights. *Nat. Nanotechnol.* **2016**, *11*, 1098−1104.

(25) Lei, L.; Huang, D.; Zeng, G.; Cheng, M.; Jiang, D.; Zhou, C.; Chen, S.; Wang, W. A Fantastic Two-Dimensional MoS_2 Material Based on the Inert Basal Planes Activation: Electronic Structure, Synthesis Strategies, Catalytic Active Sites, Catalytic and Electronic Properties. *Coord. Chem. Rev.* **2019**, *399*, 213020.

(26) Liu, H.; Lv, T.; Zhu, C.; Su, X.; Zhu, Z. Efficient Synthesis of MoS_2 Nanoparticles Modified TiO_2 Nanobelts with Enhanced Visible-Light-Driven Phtotocatalytic Activity. *J. Mol. Catal. A: Chem.* **2015**, *396*, 136−142.

(27) Li, H.; Wang, Y.; Chen, G.; Sang, Y.; Jiang, H.; He, J.; Li, X.; Liu, H. Few-Layered MoS_2 Nanosheets Wrapped Ultrafine TiO_2 Nanobelts with Enhanced Photocatalytic Property. *Nanoscale* **2016**, *8*, 6101−6109.

(28) Zheng, L.; Han, S.; Liu, H.; Yu, P.; Fang, X. Hierarchical MoS_2 Nanosheet@TiO_2 Nanotube Array Composites with Enhanced Photocatalytic and Photocurrent Performances. *Small* **2016**, *12*, 1527−1536.

(29) Guo, L.; Yang, Z.; Marcus, K.; Li, Z.; Luo, B.; Zhou, L.; Wang, X.; Du, Y.; Yang, Y. MoS_2/TiO_2 Heterostructures as Nonmetal Plasmonic Photocatalysts for Highly Efficient Hydrogen Evolution. *Energy Environ. Sci.* **2018**, *11*, 106−114.

(30) Wang, C.; Lin, H.; Liu, Z.; Wu, J.; Xu, Z.; Zhang, C. Controlled Formation of TiO_2/MoS_2 Core-Shell Heterostructures with Enhanced Visible-Light Phtotocatalytic Activities. *Part. Part. Syst. Charact.* **2016**, *33*, 221−227.

(31) Guo, N.; Zeng, Y.; Li, H.; Xu, X.; Yu, H. MoS_2 Nanosheets Encapsulating TiO_2 Hollow Spheres with Enhanced Photocatalytic Activity for Nitrophenol Reduction. *Mater. Lett.* **2017**, *209*, 417−420.

(32) Yuan, Y.-J.; Ye, Z.-J.; Lu, H.-W.; Hu, B.; Li, Y.-H.; Chen, D.-Q.; Zhong, J.-S.; Yu, Z.-T.; Zou, Z.-G. Constructing Anatase TiO_2 Nanosheets with Exposed (001) Facets/Layered MoS_2 Two-Dimensional Nanojunctions for Enhanced Solar Hydrogen Generation. *ACS Catal.* **2016**, *6*, 532−541.

(33) Hu, X.; Lu, S.; Tian, J.; Wei, N.; Song, X.; Wang, X.; Cui, H. The Selective Deposition of MoS_2 Nanosheets onto (101) Facets of TiO_2 Nanosheets with Exposed (001) Facets and their Enhanced Photocatalytic H_2 Production. *Appl. Catal., B* **2019**, *241*, 329−337.

(34) Gopal, R.; Chinnapan, M. M.; Bojarajan, A.; Rotte, N. K.; Ponraj, J. S.; Ganesan, R.; Atanas, I.; Nadarajah, M.; Manavalan, R. K.; Gaspar, J. Facile Synthesis and Defect Optimization of 2D-Layered MoS_2 on TiO_2 Heterostructure for Industrial Effluent, Wastewater Treatments. *Sci. Rep.* **2020**, *10*, 21625.

(35) Tiwari, A.; Gautam, A.; Sk, S.; Gavali, D. S.; Thapa, R.; Pal, U. Controlled Loading of MoS_2 on Hierarchical Porous TiO_2 for Enhanced Photocatalytic Hydrogen Evolution. *J. Phys. Chem. C* **2021**, *125*, 11950−11962.

(36) He, H.; Lin, J.; Fu, W.; Wang, X.; Wang, H.; Zeng, Q.; Gu, Q.; Li, Y.; Yan, C.; Tay, B. K.; Xue, C.; Hu, X.; Pantelides, S. T.; Zhou, W.; Liu, Z. MoS_2/TiO_2 Edge-On Heterostructure for Efficient Photocatalytic Hydrogen Evolution. *Adv. Energy Mater.* **2016**, *6*, 1600464.

(37) Nan, F.; Li, P.; Li, J. K.; Cai, T. Y.; Ju, S.; Fang, L. Experimental and Theoretical Evidence of Enhanced Visible Light Photoelectrochemical and Photocatalytic Properties in MoS_2/TiO_2 Nanohole Arrays. *J. Phys. Chem. C* **2018**, *122*, 15055−15062.

(38) Sun, B.; Zhou, W.; Li, H.; Ren, L.; Qiao, P.; Li, W.; Fu, H. Synthesis of Particulate Hierarchical Tandem Heterojunctions toward Optimized Photocatalytic Hydrogen Production. *Adv. Mater.* **2018**, *30*, 1804282.

(39) Li, Z.; Li, H.; Wang, S.; Yang, F.; Zhou, W. Mesoporous black $TiO_2/MoS_2/Cu_2S$ hierarchical tandem heterojunctions toward optimized photothermal-photocatalytic fuel production. *Chem. Eng. J.* 2022, 427, 131830.

(40) Wu, S.; Hu, H.; Lin, Y.; Zhang, J.; Hu, Y. H. Visible Light Photocatalytic Degradation of Tetracycline over TiO_2. *Chem. Eng. J.* 2020, 382, 122842.

(41) Yuan, Z.; Jiang, Z.-J.; Wang, Y.; Jiang, Z.; Deng, B. Photocatalytic Ag Nanoparticle Growth Induced Oxygen Vacancy Formation on Few-Layered BiOBr Nanosheets and Enhancements of $*O_2^-$ Generation Toward Tetracycline Photodegradation. *J. Phys. Chem. C* 2022, 126, 13191−13201.

(42) Hunge, Y. M.; Yadav, A. A.; Kang, S. W.; Kim, H. Photocatalytic Degradation of Tetracycline Antibiotics Using Hydro-thermally Synthesized Two-Dimensional Molybdenum Disulfide/Titanium Dioxide Composites. *J. Colloid Interface Sci.* 2022, 606, 454−463.

(43) Yang, M.; He, L.; Shi, Z.; Mei, J.; Liu, C.; Yang, B.; Cui, J.; Liang, S.; Sun, S. An Unprecedented Strategy to Fabricate Inside/Surface Homojunction in Bismuth Oxychloride for Efficient Photocatalysis. *J. Phys. Chem. C* 2023, 127, 4570−4581.

(44) Salmanzadeh-Jamadi, Z.; Habibi-Yangjeh, A.; Xu, C.; Wang, C. Anchoring $Bi_4O_5I_2$ and CDs on Brown TiO_{2-x}: S-scheme Heterojunction Mechanism for Impressive Degradation of Several Antibiotics under Visible Light. *J. Alloys Compd.* 2023, 948, 169711.

(45) Evgenidou, E. N.; Konstantinou, I. K.; Lambropoulou, D. A. Occurrence and Removal of Transformation Products of PPCPs and Illicit Drugs in Wastewaters: a Review. *Sci. Total Environ.* 2015, 505, 905−926.

(46) Toumazatou, A.; Antoniadou, M.; Sakellis, E.; Tsoutsou, D.; Gardelis, S.; Romanos, G. E.; Ioannidis, N.; Boukos, N.; Dimoulas, A.; Falaras, P.; Likodimos, V. Boosting Visible Light Harvesting and Charge Separation in Surface Modified TiO_2 Photonic Crystal Catalysts with CoO_x Nanoclusters. *Mater. Adv.* 2020, 1, 2310−2322.

(47) Hatton, B.; Mishchenko, L.; Davis, S.; Sandhage, K. H.; Aizenberg, J. Assembly of Large Area, Highly Ordered, Crack-Free Inverse Opal Films. *Proc. Natl. Acad. Sci. U.S.A.* 2010, 107, 10354−10359.

(48) Vasquez, Y.; Kolle, M.; Mishchenko, L.; Hatton, B. D.; Aizenberg, J. Three-Phase Co-Assembly: in Situ Incorporation of Nanoparticles into Tunable, Highly Ordered, Porous Silica Films. *ACS Photonics* 2014, 1, 53−60.

(49) Cai, Z.; Xiong, Z.; Lu, X.; Teng, J. In Situ Gold-Loaded Titania Photonic Crystals with Enhanced Photocatalytic Activity. *J. Mater. Chem. A* 2014, 2, 545−553.

(50) Apostolaki, M-A.; Sakellis, E.; Tsipas, P.; Giannouri, M.; Gardelis, S.; Boukos, N.; Dimoulas, A.; Likodimos, V. Three-Phase Co-Assembly of Compositionally Tunable WO_3/TiO_2 Inverse Opal Photoelectrodes. *Appl. Surf. Sci.* 2023, 613, 155919.

(51) Synnatschke, K.; Cieslik, P. A.; Harvey, A.; Castellanos-Gomez, A.; Tian, T.; Shih, C.-J.; Chernikov, A.; Santos, E. J. G.; Coleman, J. N.; Backes, C. Length- and Thickness-Dependent Optical Response of Liquid-Exfoliated Transition Metal Dichalcogenides. *Chem. Mater.* 2019, 31, 10049−10062.

(52) Apostolaki, M-A.; Toumazatou, A.; Antoniadou, M.; Sakellis, E.; Xenogiannopoulou, E.; Gardelis, S.; Boukos, N.; Falaras, P.; Dimoulas, A.; Likodimos, V. Graphene Quantum Dot-TiO_2 Photonic Crystal Films for Photocatalytic Applications. *Nanomaterials* 2020, 10, 2566.

(53) Hong, J.; Hu, Z.; Probert, M.; Li, K.; Lv, D.; Yang, X.; Gu, L.; Mao, N.; Feng, Q.; Xie, L.; Zhang, J.; Wu, D.; Zhang, Z.; Jin, C.; Ji, W.; Zhang, X.; Yuan, J.; Zhang, Z. Exploring Atomic Defects in Molybdenum Disulphide Monolayers. *Nat. Commun.* 2015, 6, 6293.

(54) Balaji, S.; Djaoued, Y.; Robichaud, J. Phonon Confinement Studies in Nanocrystalline Anatase-TiO_2 Thin Films by Micro-Raman Spectroscopy. *J. Raman Spectrosc.* 2006, 37, 1416−1422.

(55) Zhang, X.; Qiao, X. F.; Shi, W.; Wu, J. B.; Jiang, D. S.; Tan, P. H. Phonon and Raman Scattering of Two-Dimensional Transition Metal Dichalcogenides from Monolayer, Multilayer to Bulk Material. *Chem. Soc. Rev.* 2015, 44, 2757−2785.

(56) Biesinger, M. C.; Lau, L. W. M.; Gerson, A. R.; Smart, R. S. C. Resolving Surface Chemical States in XPS Analysis of First Row Transition Metals, Oxides and Hydroxides: Sc, Ti, V, Cu and Zn. *Appl. Surf. Sci.* 2010, 257, 887−898.

(57) Ganta, D.; Sinha, S.; Haasch, R. T. 2-D Material Molybdenum Disulfide Analyzed by XPS. *Surf. Sci. Spectra* 2014, 21, 19−27.

(58) Pylarinou, M.; Sakellis, E.; Tsipas, P.; Romanos, G. E.; Gardelis, S.; Dimoulas, A.; Likodimos, V. Mo-$BiVO_4$/Ca-$BiVO_4$ Homojunction Nanostructure-Based Inverse Opals for Photoelectrocatalytic Pharmaceutical Degradation under Visible Light. *ACS Appl. Nano Mater.* 2023, 6, 6759−6771.

(59) Pylarinou, M.; Toumazatou, A.; Sakellis, E.; Xenogiannopoulou, E.; Gardelis, S.; Boukos, N.; Dimoulas, A.; Likodimos, V. Visible Light Trapping Against Charge Recombination in FeO_x-TiO_2 Photonic Crystal Photocatalysts. *Materials* 2021, 14, 7117.

(60) Deparis, O.; Mouchet, S.; Su, B.-L. Light Harvesting in Photonic Crystals Revisited: why do Slow Photons at the Blue Edge Enhance Absorption? *Phys. Chem. Chem. Phys.* 2015, 17, 30525−30532.

(61) Wang, L.; Mogan, T. R.; Wang, K.; Takashima, M.; Ohtani, B.; Kowalska, E. Fabrication and Characterization of Inverse-Opal Titania Films for Enhancement of Photocatalytic Activity. *ChemEngineering* 2022, 6, 33.

(62) Michael-Kordatou, I.; Karaolia, P.; Fatta-Kassinos, D. The Role of Operating Parameters and Oxidative Damage Mechanisms of Advanced Chemical Oxidation Processes in the Combat Against Antibiotic-Resistant Bacteria and Resistance Genes Present in Urban Wastewater. *Water Res.* 2018, 129, 208−230.

(63) Nguyen, V. Q.; Mady, A. H.; Mahadadalkar, M. A.; Baynosa, M. L.; Kumar, D. R.; Rabie, A. M.; Lee, J.; Kim, W. K.; Shim, J.-J. Highly Active Z-Scheme Heterojunction Photocatalyst of Anatase TiO_2 Octahedra Covered with C-MoS_2 Nanosheets for Efficient Degradation of Organic Pollutants Under Solar Light. *J. Colloid Interface Sci.* 2022, 606, 337−352.

(64) Li, Y.; Li, H.; Lu, X.; Yu, X.; Kong, M.; Duan, X.; Qin, G.; Zhao, Y.; Wang, Z.; Dionysiou, D. D. Molybdenum Disulfide Nanosheets Vertically Grown on Self-Supported Titanium Dioxide/Nitrogen-Doped Carbon Nanofiber Film for Effective Hydrogen Peroxide Decomposition and "Memory Catalysis". *J. Colloid Interface Sci.* 2021, 596, 384−395.